Journal of ELECTRONIC MATERIALS, Vol. 49, No. 1, 2020
https://doi.org/10.1007/s11664-019-07758-7

Nanomechanical Responses of an Intermetallic Compound Layer in Transient Liquid Phase Bonding Using Indium

JENN-MING SONG,[1,3,4,5] WEI-CHIH LU,[2] and PEI-WEN CHOU[1]

1.—Department of Materials Science and Engineering, National Chung Hsing University, Taichung, Taiwan. 2.—Department of Materials Science and Engineering, National Dong Hwa University, Hualien, Taiwan. 3.—Research Center for Sustainable Energy and Nanotechnology, National Chung Hsing University, Taichung, Taiwan. 4.—Innovation and Development Center of Sustainable Agriculture, National Chung Hsing University, Taichung, Taiwan. 5.—e-mail: samsong@nchu.edu.tw

Low-temperature transient liquid phase bonding (TLPB) can be achieved using indium, and the joints thus formed can withstand high temperatures. Since the joints that are formed with TLPB entirely consist of intermetallic compounds (IMCs), this study investigates the phase evolution and mechanical properties of IMCs that are obtained from isothermal reactions between In and commonly used substrate metals, Cu, Ag and Au. Using nanoindentation, the relationships between the yield strain, work hardening exponent and strain rate sensitivity of In-bearing and other frequently observed IMC phases were compared. Notably, the strain-induced precipitation of Ag_3In occurred in the indent of Ag_9In_4.

Key words: transient liquid phase bonding (TLPB), intermetallic compounds, nanoindentation

INTRODUCTION

A considerable demand exists for electromechanical devices that are capable of operating at high temperatures,[1] such as in hybrid electric vehicles, which combine a gasoline engine with an electric motor that is equipped with built-in inverters to control the flow of electric current. Those inverters include power modules with an array of power ICs that can be operated at high temperatures. Solders with high Pb content are widely used as die-attachment materials for power semiconductor packaging. However, the RoHS restriction requires complete elimination of Pb from electronic appliances. Pb-free alternatives have been urgently sought, and several candidates have already been proposed; they include, Bi-based, Au-based and Zn-based alloys, nano-Ag pastes, and anisotropic conductive films.[1–7] Among these, Au-based solders have the shortcomings of high price, poor workability and inferior wetting, so they are unlikely to replace high Pb solders. Bi-based solders are brittle and suffer from poor electrical and thermal conductivities. Nano Ag pastes are expensive.

Transient liquid phase bonding (TLPB), which is also known as solid–liquid interdiffusion bonding (SLID) or diffusion soldering, has been extensively used in the fabrication of interconnects for high temperature applications using low-temperature processes.[8–10] Tin and indium are two commonly used joint materials for TLPB. In has a relatively low melting temperature (156.6°C), allowing it to react with substrates at low temperatures to form intermetallic phases that tolerate high temperatures.

The isothermal reactions of Au-In, Ag-In and Cu-In have been thoroughly investigated. Isothermal heating at temperatures from 150°C to 250°C yields $AuIn_2$ as the main reaction product.[11–15] The formation of AuIn, Au_7In_3, or even $Au_{10}In_3$ has also been reported.[11,16] When the Ag-In system is isothermally held at 180–250°C, $AgIn_2$ and Ag_9In_4

(Received May 12, 2019; accepted October 22, 2019; published online November 6, 2019)

are the two major IMC phases that are observed.[17–21] With respect to Cu-In, $Cu_{11}In_9$ is the stable phase at 260°C and below, while Cu_2In and Cu_7In_3 are the stable phases at higher temperatures or following long reactions.[22–26]

Since the joints that are formed by TLPB typically comprise only IMCs, comprehensive knowledge of the mechanical characteristics of IMCs is crucial for ensuring joint reliability. Consequently, nanoindentation has been used to probe the mechanical properties of IMCs at joint interfaces mainly because they have a small area.[27–31] In the depth sensing indentation technique, a constant load is applied during testing, and the penetration of the indenter tip into the sample surfaces is continuously recorded. The hardness and Young's modulus during indentation are obtained and the substrate effect is thereby prevented. Following our preliminary investigation,[32] the phase evolution and mechanical properties of IMCs that formed between In and metallic substrates were systematically examined in this report. Along with Cu, two other substrate materials in TLPB, Au and Ag, were also selected.

EXPERIMENTAL PROCEDURES

Polished coupons of pure Cu, Au and Ag with dimensions 5 mm × 5 mm × 300 μm were prepared as substrates. In films with a thickness of 2 μm were deposited on the substrates using thermal evaporation. The samples, denoted as In/Cu, In/Au and In/Ag, were isothermally heated at 180°C in a vacuum. A scanning electron microscope (SEM) (Hitachi S-3500H) that was equipped with an energy dispersive spectrometer (EDS) was used for microstructural observation. The phases of the reaction products were identified using grazing incidence x-ray diffraction (GIXRD) with an incidence angle of 1° at a scanning rate of 3° per min from 20° to 85°.

A series of IMCs were prepared to compare their mechanical properties; they were Cu-based (Cu-Sn and Cu-Zn), Ag based (Ag-Sn and Ag-Zn), Au-based (Au-Sn and Au-Zn) and Ni_3Sn_4 IMCs. The synthetic procedures have been described elsewhere.[29,30]

The mechanical performance of the intermetallic phases was determined by nanoindentation. An MTS Nanoindenter XP equipped with a continuous stiffness measurement (CSM) technique was used. The indenter maintained constant strain rates of 3×10^{-4} s^{-1}, 10^{-2} s^{-1}, and 10^{-1} s^{-1}, and the loading continued until a total indenter displacement of 300 nm was reached. The obtained load–displacement data were analyzed using the method of Oliver and Pharr[33] to determine the hardness and elastic modulus as functions of the displacement of the indenter. Each datum was the average of at least ten tests.

The plastic properties of the IMCs, such as the yield strength and work hardening exponent, were obtained using the model that was proposed by Dao et al.[34] The properties of a material are extracted from the indentation load–displacement curve.

The relationship between load and displacement during indentation can be obtained using Kick's law.

$$P = Ch^2 \tag{1}$$

where P is the indentation load; h is the indentation depth, and C is a constant, given by

$$C = \sigma_{0.033} \Pi_1 \left(\frac{E_r}{\sigma_{0.033}} \right) \tag{2}$$

where $\sigma_{0.033}$ is the representative stress at a plastic strain of 0.033 determined by the geometry of indenter, Π_1 is a dimensionless function, and E_r is the reduced modulus. The relationship between

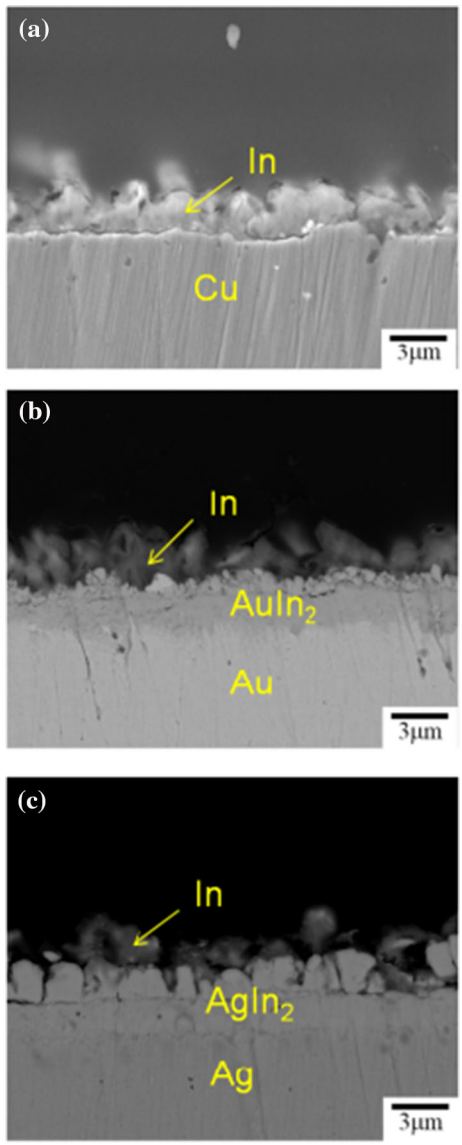

Fig. 1. In deposits on different substrates: (a) Cu, (b) Au, and (c) Ag.

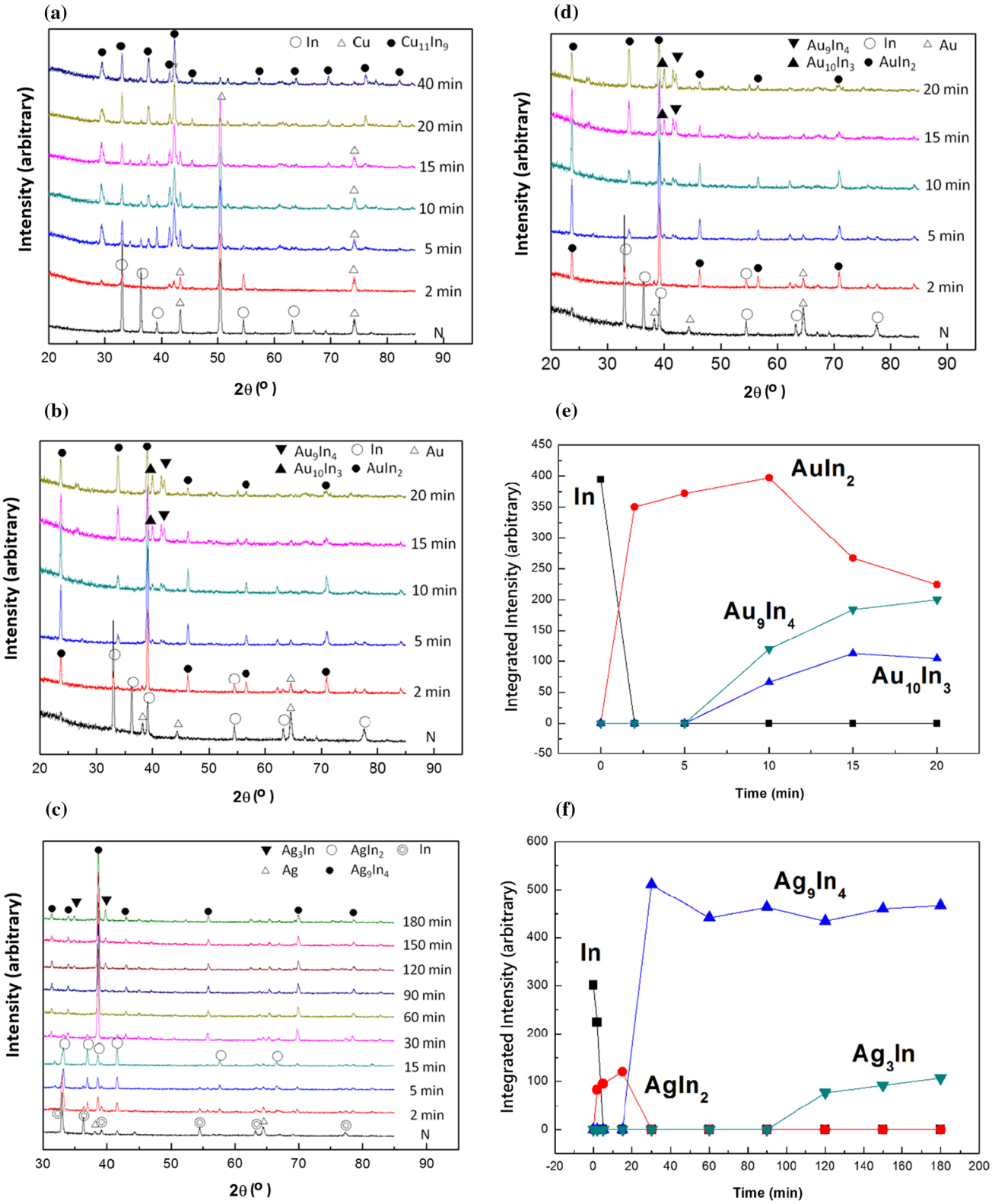

Fig. 2. XRD patterns of the samples subjected to different holding times at 180°C and the variation in main diffraction intensity of the structural phases: (a, d) In/Cu, (b, e) In/Au, and (c, f) In/Ag.

representative stress and yield stress is then given by

$$\sigma_{0.033} = \sigma_y \left(1 + 0.033 \frac{E}{\sigma_y}\right)^n \quad (3)$$

where E is the Young's modulus and n is the work hardening exponent. The work hardening exponent, which is calculated as

$$\frac{1}{E_r h_m} \frac{dP}{dh}\bigg|_{h_m} = \Pi_2 \left(\frac{E_r}{\sigma_{0.033}}, n\right) \quad (4)$$

where h_m is the maximum indentation depth; $\frac{dP}{dh}\big|_{h_m}$ is the slope of unloading, and Π_2 is a dimensionless function.

RESULTS AND DISCUSSION

Figure 1 shows the as-deposited In films on different substrates, and reveals that a portion of the In coating that is adjacent to the substrate transformed into IMCs, except in the case of In/Cu. The XRD patterns of the non-heat-treated samples in Fig. 2 do not reveal this fact owing to the shallowness of detection using GIXRD. The formation of IMCs permits interdiffusion and interactions between In deposits and the substrate during deposition.

The structural phases close to the sample surface that are subjected to different aging durations are identified from XRD patterns in Fig. 2a, b, and c. The integrated intensity of the major diffraction peak for each structural phase, shown in Fig. 2d, e, and f reveals that after a short period of isothermal heating, IMCs rapidly emerged in the sub-surface region of the deposits and that the types of IMC changed during aging at 180°C. After 5 min of aging, the In coating of In/Cu had been completely consumed, and a single IMC phase, $Cu_{11}In_9$, remained. For In/Au, In was exhausted in 2 min and $AuIn_2$ was detected. After isothermal heating for 5 min, the reaction layer comprised a mixture of $AuIn_2$, $Au_{10}In_3$ and Au_9In_4. Apparently, $AuIn_2$ was the predominant phase. For In/Ag, the first emerging IMC phase was $AgIn_2$, but it completely turned into Ag_9In_4 as a result of heating for 30 min. Ag_9In_4

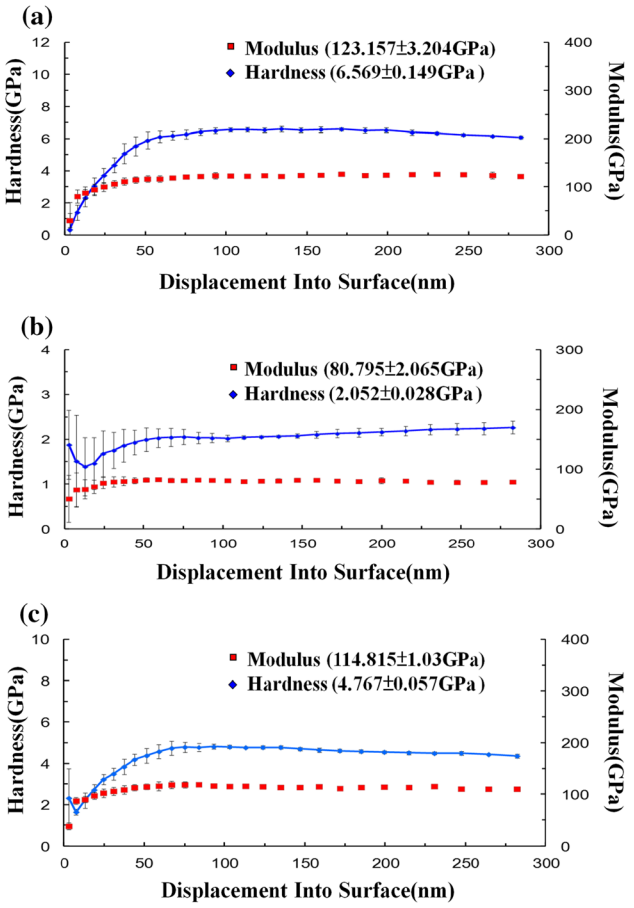

Fig. 3. Variation in hardness and elastic modulus of intermetallic compounds against penetration depth into the surface: (a) $Cu_{11}In_9$, (b) $AuIn_2$ and (c) Ag_9In_4.

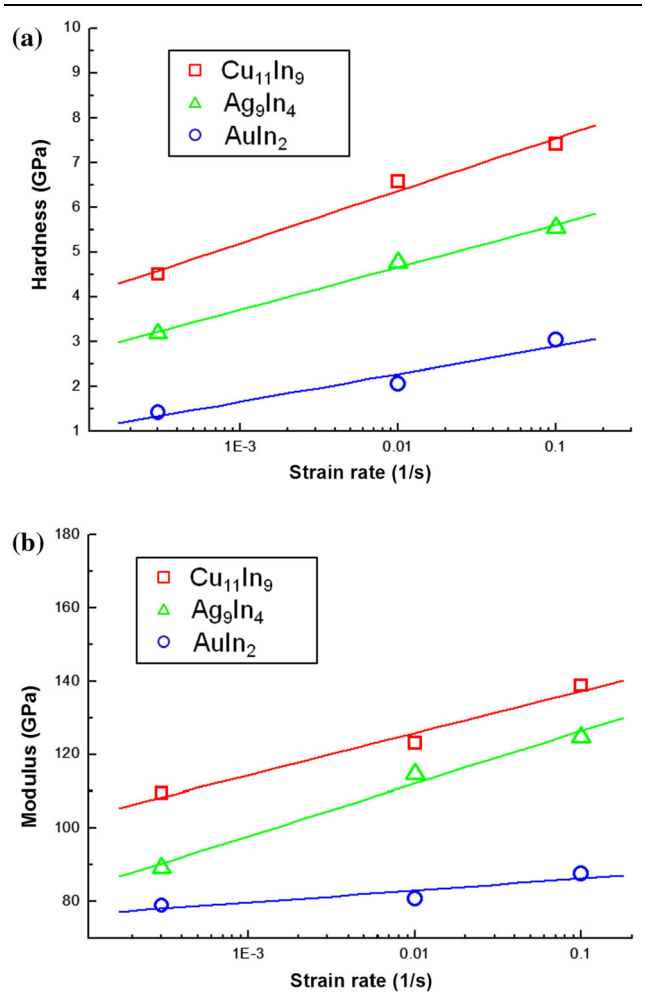

Fig. 4. Nanoindentation responses of In-based IMCs obtained under different strain rates: (a) hardness and (b) elastic modulus.

Table I. Hardness (*H*) and Young's modulus (*E*) obtained from nanoindentation test with different strain rates, as well as the strain rate sensitivity (*m*)

	3×10^{-4} s^{-1}		10^{-2} s^{-1}		10^{-1} s^{-1}		
	H **(GPa)**	***E*** **(GPa)**	***H*** **(GPa)**	***E*** **(GPa)**	***H*** **(GPa)**	***E*** **(GPa)**	***m***
$Cu_{11}In_9$	4.50 ± 0.25	109.5 ± 0.84	6.57 ± 0.15	123.2 ± 3.20	7.4 ± 0.2	138.9 ± 1.42	0.088
Ag_9In_4	3.18 ± 0.22	89.35 ± 2.22	4.77 ± 0.06	114.8 ± 1.03	5.541 ± 0.23	124.8 ± 2.12	0.098
$AuIn_2$	1.42 ± 0.05	78.93 ± 0.76	2.05 ± 0.03	80.8 ± 2.065	3.041 ± 0.27	87.66 ± 12.3	0.129
Cu_6Sn_5	5.2 ± 0.15	110 ± 3.1	7.3 ± 0.08	130 ± 2.13	8.3 ± 0.23	139 ± 2.61	0.082
Cu_3Sn	5.1 ± 0.06	140 ± 2.1	7.2 ± 0.21	160 ± 3.78	8.2 ± 0.13	175 ± 3.31	0.083
Ag_3Sn	1.7 ± 0.12	72 ± 4.12	2.8 ± 0.12	90 ± 3.86	3.2 ± 0.17	108 ± 4.42	0.112
$AuSn_2$	1.2 ± 0.09	68 ± 3.5	2.1 ± 0.12	99 ± 2.1	2.6 ± 0.04	106 ± 2.6	0.135
$AuSn_4$	0.4 ± 0.02	31 ± 0.4	0.7 ± 0.07	34 ± 0.5	0.9 ± 0.04	36 ± 0.6	0.141
Ni_3Sn_4	3.7 ± 0.09	127 ± 2.9	4.5 ± 0.13	145 ± 5.9	5.9 ± 0.21	159 ± 1.6	0.081
Cu_5Zn_8	4.9 ± 0.02	170 ± 2.2	6.9 ± 0.09	192 ± 1.46	8.3 ± 0.11	215 ± 4.21	0.091
AgZn	2.3 ± 0.26	96 ± 2.11	3.4 ± 0.08	117 ± 1.28	3.9 ± 0.21	126 ± 2.54	0.093
Ag_5Zn_8	3.0 ± 0.12	97 ± 2.68	4.8 ± 0.15	124 ± 3.74	5.6 ± 0.19	143 ± 1.67	0.109
$AuZn_3$	1.3 ± 0.03	111 ± 2.3	2.2 ± 0.07	133 ± 2.5	2.7 ± 0.12	141 ± 1.6	0.127

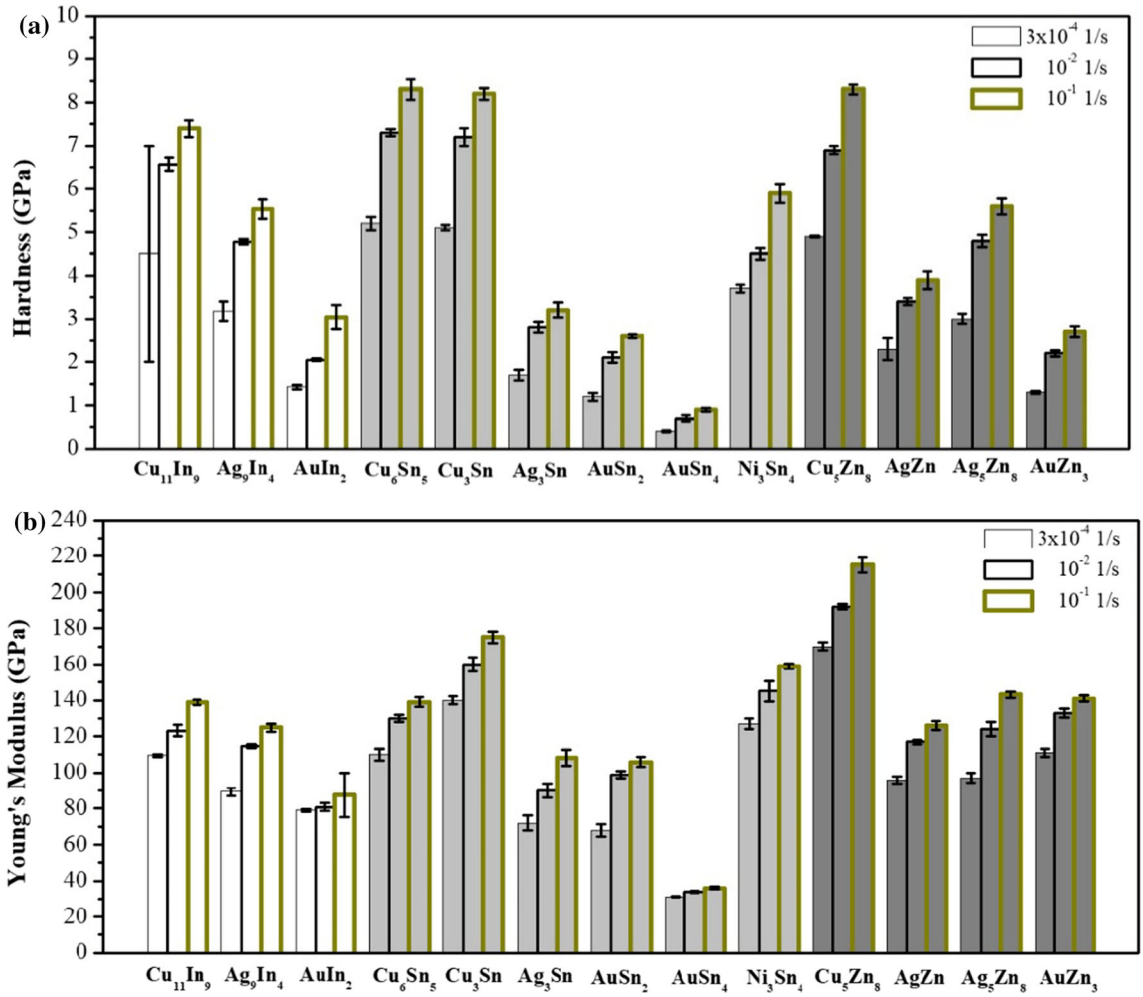

Fig. 5. Nanoindentation responses of commonly observed IMCs at solder joint interfaces under different strain rate conditions: (a) hardness, and (b) Young's modulus.

was the main structural phase that was present thereafter, but a small amount of Ag_3In was detected following aging for 1.5 h.

To obtain the mechanical properties of the major IMC phases, the heating conditions for the nanoindentation testing samples were set from the

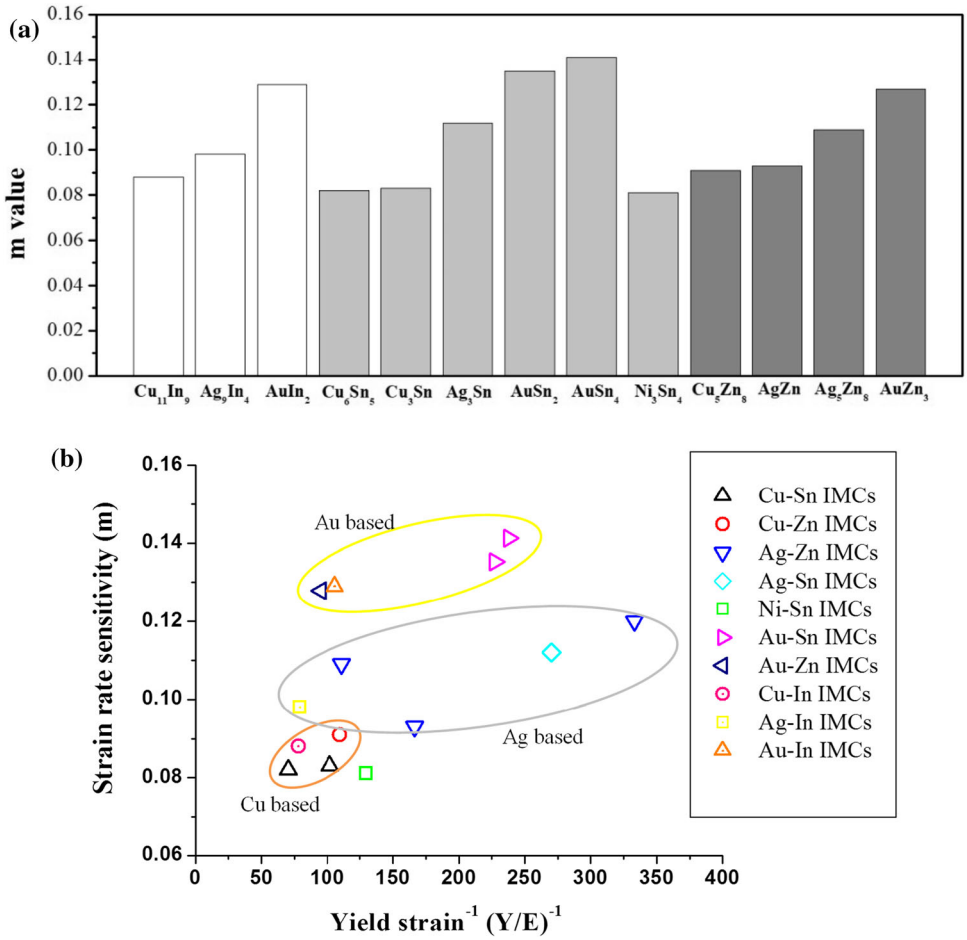

Fig. 6. (a) Strain rate sensitivities (m values) of commonly observed IMCs and (b) their relationship with $(Y/E)^{-1}$ in terms of IMC groups.

quantitative data in Fig. 2d, e, and f. In 40 min-aged In/Cu, 5 min-aged In/Au and 30 min-aged In/Ag, single phases of $Cu_{11}In_9$, $AuIn_2$ and Ag_9In_4 were respectively detected. The indentations were made perpendicular to each sample surface. The indenter was pressed up to 300 nm into the specimen, and the hardness and the elastic modulus were continuously recorded as functions of the displacement of the indenter. Examples of which are displayed in Fig. 3. After an initial transient stage, the measured hardness and elastic modulus during the indent penetration remained almost constant, revealing the homogeneity of the structural phase in the testing range. To collect stable data and to eliminate substrate effect, the hardness and Young's modulus that were recorded at penetration depths from 100 nm to 150 nm were used.

Figure 4a and b plot the hardness and elastic modulus of the In-bearing IMCs that were tested at various strain rates, indicating that the obtained data increased with the strain rate, and the increases varies among the IMC phases. At the same strain rate, $Cu_{11}In_9$ had a higher hardness and Young's modulus than Ag_9In_4, which had a higher hardness and Young's modulus than $AuIn_2$. Table I presents the quantitative data and Fig. 5 compares those data with those of other IMCs, which are frequently observed at solder joint interfaces. For all IMCs, hardness and Young's modulus increased with the strain rate. Regardless of whether they contained In, Sn or Zn, Cu-based IMCs had greater hardness and Young's moduli than Ag-based IMCs, which had greater hardness and Young's moduli than Au-based IMCs.

The strain rate sensitivity m, which quantifies the dependence of strain rate on mechanical characteristics was defined as follows[35]

$$m = \frac{\mathrm{d}\ln H}{\mathrm{d}\ln \dot{\varepsilon}} \tag{5}$$

where H is the hardness measured at various strain rates.

Table I and Fig. 6a show that the m value varied differently from the aforementioned hardness and modulus. The softest IMC phases, Au-based IMCs, had the highest m values. Figure 6b plots m as a function of Y (yield strength)/E (elastic modulus), which is the so-called yield strain, i.e. the strain corresponding to the yield strength. Table II presents the yield strength and work hardening exponent that were obtained using Eqs. 1–4. The term $Y/$

Table II. Young's modulus and work hardening exponent

Phase	Yield strength (MPa)	Work hardening exponent (n)
$Cu_{11}In_9$	1471.8 ± 143.6	0.085 ± 0.058
$AuIn_2$	764.4 ± 22.2	0.072 ± 0.006
Ag_9In_4	1398.8 ± 103.4	0.083 ± 0.003
Cu_6Sn_5	1850.6 ± 123.9	0.105 ± 0.010
Cu_3Sn	1440.3 ± 260.4	0.075 ± 0.001
Cu_5Zn_8	1753.2 ± 19.2	0.074 ± 0.0006
Ag_3Sn	334.1 ± 39.1	0.056 ± 0.002
AgZn	698.3 ± 16.0	0.064 ± 0.0005
Ag_5Zn_8	1214.2 ± 64.5	0.074 ± 0.0005
$AuZn_3$	1365.5 ± 27.8	0.076 ± 0.002
$AuSn_2$	420.0 ± 71.0	0.058 ± 0.003
$AuSn_4$	143.8 ± 13.1	0.057 ± 0.001
Ni_3Sn_4	1125.1 ± 46.8	0.070 ± 0.001

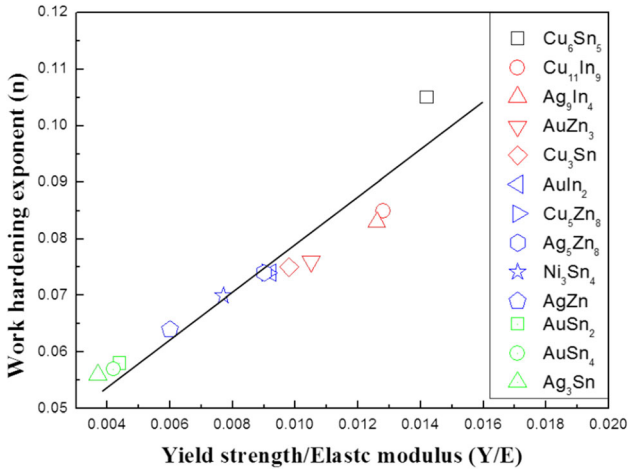

Fig. 7. The relationship between work hardening exponent and (*Y*/*E*) for various kinds of IMCs.

E is inversely proportional to the plastic deformability of a material.[29–31,36] A higher $(Y/E)^{-1}$ implies greater plasticity. With respect to In-containing IMCs, as shown in Fig. 6b, $AuIn_2$ had a higher $(Y/E)^{-1}$ than both $Cu_{11}In_9$ and Ag_9In_4, indicating that it was more plastically deformable.

As presented in Fig. 6b, IMCs of a particular Cu-based, Ag-based, Au-based and Ni-based, m increased with $(Y/E)^{-1}$, interestingly revealing that a highly plastically deformable IMC is strengthened more at a higher strain rate. Figure 6b also reveals that the m values decrease in the order Au-based > Ag-based > Cu based. Ni_3Sn_4 behaved almost the same strain rate sensitivity as Cu based IMCs, but it was more plastic deformable. All Cu-based IMCs had a relatively low $(Y/E)^{-1}$, indicating a lack of plastic deformability and, therefore, a brittle nature. Cu-based IMCs exhibited a slightly stronger dependence of $(Y/E)^{-1}$ on m than Ag and Au-based IMCs.

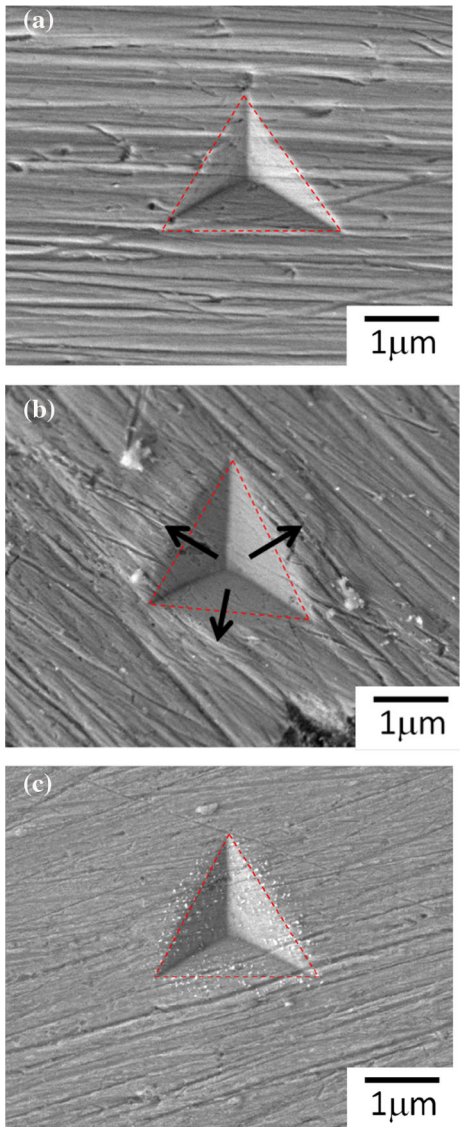

Fig. 8. The indents on the In-bearing IMCs: (a) $Cu_{11}In_9$, (b) $AuIn_2$ and (c) Ag_9In_4.

The n values of all IMCs (Table II) are directly proportional to *Y*/*E*, the yield strain, as shown in Fig. 7, suggesting that work hardening and plastic deformability vary oppositely. The work hardening exponent of $AuIn_2$ was smaller than that of Ag_9In_4, which was similar to that of $Cu_{11}In_9$.

Figure 8 shows the indent morphologies of the IMCs. As illustrated in Fig. 8a and c, $Cu_{11}In_9$ and Ag_9In_4 exhibit a perfect indent with no inhomogeneous plastic deformation feature, such as crack, pile-up, or sink-in). In contrast, pile-ups were observed at the edge of the indent in $AuIn_2$ (Fig. 8b), indicating its superior plastic deformability. Remarkably, numerous tiny precipitates were observed at and in the proximity of the indent impression in Ag_9In_4 (Fig. 8c). Instead of Ag_2In,[16–19] those nano-sized particles could be referred to Ag_3In that was formed by strain-induced precipitation in

the Ag_9In_4 matrix, according to the XRD results. This phenomenon did not occur in $AuIn_2$ because of the difference in lattice parameters between the precipitates and the matrix. With respect to In/Ag, the precipitates of Ag_3In have a smaller lattice constant (0.2299 nm) than the Ag_9In_4 matrix (0.992 nm), so the precipitation of Ag_3In caused the relaxation of compressive strain, and so was accelerated by nanoindentation. However, the lattice constants of both $Au_{10}In_3$ and Au_9In_4 (1.0538 nm and 0.9829 nm respectively) are larger than that of $AuIn_2$ (0.6517 nm). Pre-existing compressive strain limited this form of precipitation.

CONCLUSIONS

In summary, the phase transitions and nanoindentation responses of In deposits on substrates of Cu, Ag and Au, subjected to aging at 180°C were studied. Experimental results revealed that the main reaction products were $Cu_{11}In_9$ for the In/Cu samples, Ag_9In_4 for In/Ag samples, and $AuIn_2$ for the In/Au samples. The hardness and Young's modulus of $Cu_{11}In_9$ were greater than those of Ag_9In_4, which exceeded those of $AuIn_2$. Moreover, $AuIn_2$ exhibited the strongest dependence of strain rate on mechanical properties (i.e. strain rate sensitivity) and the lowest work hardening. A comparison with other IMCs was also made. Observation of the indent morphology revealed that perfect indents on the $Cu_{11}In_9$ and Ag_9In_4 samples. Pile-ups at the corner of the indent impression in $AuIn_2$ were observed owing to its relatively high plastic deformability. Notably, strain-induced precipitation of $AgIn_3$ was observed at the indents in Ag_9In_4.

ACKNOWLEDGMENTS

This work was supported by the Ministry of Science and Technology (Taiwan) through Grant MOST 106-2221-E-005-028-MY3, for which the authors are grateful. This work was also supported by the "Innovation and Development Center of Sustainable Agriculture" from the Featured Research Center Program within the framework of the Higher Education Sprout Project by the Ministry of Education (Taiwan, R.O.C.).

REFERENCES

1. H.S. Chin, K.Y. Cheong, and A.B. Ismail, *Metall. Mater. Trans.* 41, 824 (2010).
2. J.G. Bai, J. Yin, Z. Zhang, G.Q. Lu, and J.D. Wyk, *IEEE Trans. Adv. Packag.* 30, 506 (2007).
3. K. Suganuma, S.J. Kim, and K.S. Kim, *JOM* 61, 64 (2009).
4. S.J. Kim, K.S. Kim, K. Suganuma, and G. Izuta, *J. Electron. Mater.* 38, 873 (2009).
5. S. Zhang, S.H. Kim, T.W. Kim, Y.S. Kim, and K.W. Paik, *IEEE Trans. Compon. Packag. Manuf. Technol.* 5, 9 (2015).
6. S. Zhang and K.W. Paik *IEEE Trans. Compon. Packag. Manuf. Technol.* 6, 216 (2016).
7. S. Zhang, M. Yang, Y. Wu, J. Du, T. Lin, P. He, M. Huang, and K.W. Paik, *IEEE Trans. Compon. Packag. Manuf. Technol.* 8, 383 (2018).
8. W.C. Warren III, J. Chae, and K. Najafi, *IEEE Trans. Adv. Packag.* 28, 643 (2005).
9. Y.Y. Wu and C.C. Lee, *IEEE Trans. Compon. Packag. Manuf. Technol.* 3, 711 (2013).
10. C.C. Lee, S.J. Hsu, and Y.Y. Wu, *J. Electron. Mater.* 43, 9 (2014).
11. W. Zhang and W. Ruythooren, *J. Electron. Mater.* 37, 1095 (2008).
12. H.A. Mustain, W.D. Brown, and S.S. Ang, *IEEE Trans. Compon. Packag. Technol.* 33, 563 (2010).
13. T.T. Luu, N. Hoivik, K. Wang, K.E. Aasmundtveit, and A.S.B. Vardøy, *Metall. Mater. Trans. A* 46, 2637 (2015).
14. W.W. So and C.C. Lee, *IEEE Trans. Compon. Packag. Technol.* 23, 377 (2000).
15. L. Deillon, T. Hessler, A. Hessler-Wyser, and M. Rappaz, *Acta Mater.* 79, 258 (2014).
16. J. Lian, J.W. Chun, M.S. Goorsky, and J. Wang, *J. Mater. Sci.* 44, 6155 (2009).
17. R.I. Made, C.L. Gan, L.L. Yan, A. Yu, S.W. Yoon, J.H. Lau, and C. Lee, *J. Electron. Mater.* 38, 365 (2009).
18. P.J. Wang, C.H. Sha, and C.C. Lee, *IEEE Trans. Compon. Packag. Technol.* 33, 462 (2010).
19. S.J. Hsu, C.C. Lee, *ECTC.* (2015), p. 1247.
20. W.P. Lin and C.C. Lee, *IEEE Trans. Compon. Packag. Manuf. Technol.* 1, 1311 (2011).
21. Y.Y. Wu, D. Nwoke, F.D. Barlow, and C.C. Lee, *IEEE Trans. Compon. Packag. Manuf. Technol.* 4, 1420 (2014).
22. K.A. Lindahl, J.J. Moore, D.L. Olson, R. Noufi, and B. Lanning, *Thin Solid Films* 290, 518 (1996).
23. D.G. Kim, C.Y. Lee, and S.B. Jung, *J. Mater. Sci.: Mater. Electron.* 15, 95 (2004).
24. Y.S. Chien, Y.P. Huang, R.N. Tzeng, M.S. Shy, T.H. Lin, K.H. Chen, C.T. Chiu, C.T. Chuang, W. Hwang, J.C. Chiou, H.-M. Tong, and K.N. Chen, *IEEE Trans. Electron. Devices* 61, 1131 (2014).
25. Y. Tian, N. Wang, Y. Li, C. Wang, *13th ICEPT-HDP* (2012), p. 216.
26. X. Zhao, Y. Tian, N. Wang, *14th ICEPT* (2013), p. 143.
27. X. Deng, N. Chawla, K.K. Chawla, and M. Koopman, *Acta Mater.* 52, 4291 (2004).
28. J.M. Song, Y.L. Shen, C.W. Su, Y.S. Lai, and Y.T. Chiu, *Mater. Trans.* 50, 1231 (2009).
29. J.M. Song, C.W. Su, Y.S. Lai, and Y.T. Chiu, *J. Mater. Res.* 25, 629 (2010).
30. J.M. Song, B.R. Huang, C.Y. Liu, Y.S. Lai, Y.T. Chiu, and T.W. Huang, *Mater. Sci. Eng., A* 534, 53 (2012).
31. J.Y. Wu, Y.S. Chiu, Y.W. Wang, and C.R. Kao, *Mater. Sci. Eng., A* 753, 22 (2019).
32. J.M. Song, W.C. Lu, *International Conference on Electronic Packaging* (ICEP) (2014), pp. 640–643.
33. W.C. Oliver and G.M. Pharr, *J. Mater. Res.* 564, 1564 (1992).
34. M. Dao, N. Chollacoop, K.J.V. Vliet, T.A. Venkatesh, and S. Suresh, *Acta Mater.* 49, 3899 (2001).
35. C. Fisher-Cripps, *Nanoindentation*, 2nd ed. (New York: Springer, 2004), p. 146.
36. Y.V. Milman, B.A. Galanov, and S.I. Chugunova, *Acta Mater.* 41, 2523 (1993).